# Jet impingement onto a cavity



B.S. Yilbas, S.Z. Shuja and M.O. Budair
*ME Department, KFUPM, Dhahran, Saudi Arabia*

***Keywords*** *Jets, Heat transfer*

Received January 2002
Accepted May 2002

***Abstract*** *Jet impingement onto surface finds wide application in industry. In laser processing an assisting gas jet is introduced either to shield the surface from oxidation reactions or initiating exothermic reaction to increase energy in the region irradiated by a laser beam. When an impinging gas jet is used for a shielding purpose, the gas jet enhances the convective cooling of the cavity surface. The convective cooling of the laser formed cavity surface can be simulated through jet impingement onto a cavity with elevated wall temperatures. In the present study, gas impingement onto a slot is considered. The wall temperature of the cavity is kept at elevated temperature similar to the melting temperature of the substrate material. A control volume approach is used to simulate the flow and temperature fields. The Reynolds Stress Turbulence model (RSTM) is employed to account for the turbulence. To examine the effect of cavity depth on the heat transfer characteristics, the depth is varied while keeping the cavity width constant. It is found that impinging jet penetrates into a cavity, which in turn, results in a stagnation region extending into the cavity. An impinging gas jet has considerable effect on the Nusselt number along the side walls of the cavity while the Nusselt number monotonically changes with varying cavity depth.*

## Nomenclature

$H$ = enthalpy
$K$ = thermal conductivity
$k$ = turbulent kinetic energy
$p$ = pressure
$P$ = rate of production
$R_{ij}$ = Reynolds stress
Re = Reynolds Number
$r$ = distance in the radial direction
$t$ = time
$T$ = temperature
$u^*$ = friction velocity
$U$ = arbitrary velocity
$\forall$ = volume
$x$ = distance in the axial direction
$x_n$ = distance to the nearest wall
$x_{max}$ = distance to the solid rear surface

*Greek symbols*

$\alpha$ = thermal diffusivity
$\Gamma$ = arbitrary diffusion coefficient
$\epsilon$ = energy dissipation
$\lambda$ = turbulence intensity
$\mu$ = dynamic viscosity
$\nu$ = kinematic viscosity
$\rho$ = density (function of temperature and pressure for gas)
$\sigma$ = variable Prandtl No.
$\Phi$ = viscous dissipation
$\phi$ = arbitrary variable
$\Pi$ = energy transport due to pressure excluding strain interactions
$\Pi_w$ = energy transport due to wall reflection
$\Lambda$ = energy transport by diffusion

*Subscripts*

amb = ambient
$i, j$ = arbitrary direction
jet = gas jet at inlet
l = laminar
$p$ = a typical node in the computational grid
t = turbulent
n,s,e,w,l,h = north, south, east, west, low or high node
$w$ = wall

The authors acknowledge the support of King Fahd University of Petroleum and Minerals. Dhahran, Saudi Arabia for this work.

International Journal of Numerical Methods for Heat & Fluid Flow, Vol. 12 No. 7, 2002, pp. 817-838.

DOI 10.1108/09615530210443043

## 1. Introduction

Jet impingement onto metallic cavities finds applications in process industry. One of the examples of such applications is forming and heating of surfaces by high energy beams. When a high power laser beam interacts with a metallic substrate, a phase change process results and a cavity is formed, which is deep in size with an almost fixed width. Moreover, in a laser processing of solid substrates, an assisting gas is introduced, in general, co-axially with the laser beam. The assisting gas has twofold effects: i) an inert assisting gas shields the heated area preventing from high temperature oxidation reaction, or ii) it generates a high temperature exothermic reaction increasing the thermal energy in the section under the laser processing. Consequently, the effect of an assisting gas on the heating mechanism needs to be included in the analysis during a laser processing of substrate materials. In the laser processing, a cavity wall temperature remains almost at the melting temperature of the substrate material. Therefore, the heating model can be simplified by assuming a fixed cavity geometry with a constant wall temperature. Moreover, the process can be considered as steady, since the processing conditions remain the same as in the case of the laser cutting of solid substrates.

Considerable research studies were carried out to explore the laser cutting process. The analysis of laser cutting was introduced by Gonsalves and Duley (1972). A turbulent boundary layer approach allowing reaction for $CO_2$ laser oxygen-assisted cutting was studied by Yilbas and Sahin (1994). They indicated that the total chemical reaction contribution increases at low laser cutting speeds and high oxygen jet velocities. The cut width did not change considerably once the cutting parameters were set. Laser grooving and cutting processes were examined by Sheng and Chryssolouris (1994). They introduced laser cutting and grooving schemes for improved product quality. Aloke *et al.* (1997) investigated the dimensional tolerances of laser cut holes in mild steel thin blades. They showed that there was an excellent correlation between the model proposed and experimental data specially for smaller diameter holes. The scaling laws for thick-section cutting with a chemical oxygen-iodine laser was investigated by Kar *et al.* (1997). The effects of various process parameters, such as laser power, spot size, cutting speed and cutting gas velocity on the cutting depth were discussed. They indicated that the comparison of mathematical model and experimental results enabled to determine the effective absorptivity during laser materials processing. The laser cutting process and striations were examined by Yilbas (1997). He showed that the mathematical model represented the physical phenomena well within the limits of the characteristic distance. The assisting gas composition effect on the $CO_2$ laser cutting of mild steel was studied by Chen (1998). He showed that a high purity of oxygen was required for the high-performance $CO_2$ laser cutting of mild steel. Laser cutting of metallic-coated sheet steels was investigated by Prasad *et al.* (1998). They indicated that the cutting speed was a function of the

input power and that the laser processing of the coated surfaces was a commercially viable option.

In laser gas assisting processing, a gas jet impinges onto laser produced cavity. Due to the heat transfer rates between the high temperature cavity wall and relatively cool impinging gas, thermodynamic pressure is built up close to the cavity surfaces. Moreover, the stagnation flow situation in the cavity generates a pressure field in this region. Consequently, the effect of fluid and thermodynamic pressure built up in the cavity modifies the flow conditions and heat transfer rates. Consequently, when modeling the gas-jet effect on the heat transfer rates in the cavity, the equation of state governing the thermodynamics process in the region should be accommodated. Considerable research studies were conducted to explore the gas-jet impingement and heat transfer. The turbulence models for near-wall and low Reynolds number flows were examined by Patel *et al.* (1985). The systematic evaluation of two-equation low Reynolds number turbulence models were presented. The stagnation turbulent flows were studied by Strahle *et al.* (1987). They indicated that at high Reynolds number, the effect of the stagnation process was that the nonviscous zone outside the boundary layer predicted an excessive effect of body size on the results, although, the agreement was still satisfactory. Heat transfer measurements from a plane surface due to uniform heat flux and jet impingement were carried out by Baughn and Shimizu (1989). They indicated that the maximum heat transfer rates extended into the regions in the radial direction of the stagnation region. Jambunathan *et al.* (1992) examined the heat transfer rates from a flat plate due to a single circular jet impingement. They indicated that the Nusselt number was independent of nozzle-to-plate spacing up to a value of twelve nozzle diameters at radii greater than six nozzle diameters from the stagnation point. The Reynolds Stress Turbulence Model (RSTM) assessment using round jet data was carried out by Lasher and Taulbee (1994). They indicated that predictions using the linear models were generally as good as those obtained using nonlinear models. A numerical study was carried out by Hosseinalipour and Mujumdar (1995) to predict and compare the fluid flow and heat transfer characteristics of two-dimensional turbulent confined impinging and opposing jet flows. They indicated that opposing turbulent jets could provide a more uniform distribution of the Nusselt number along the confining channel walls than the single turbulent impinging jet. The local heat transfer coefficient distribution on a square heat source due to different jet configurations was investigated by Morris *et al.* (1996). They showed that the stagnation and average heat transfer coefficients predicted agreed with experimental results within a maximum deviations of 16 and 20 percent, respectively. The laser gas assisted heating was studied by Shuja *et al.* (1998). The study was dealt with conduction limited heating case. They indicated that as the radial distance from the heated spot center increased, the temperature at the surface decreased rapidly. Moreover, Shuja

and Yilbas (2000) examined the influence of gas jet velocity in laser heating process for a moving workpiece case. They showed that the movement of the workpiece affected the location of the maximum temperature at the surface, which moved away from the initially irradiated spot center in the direction of workpiece motion.

In light of the above arguments, the present study is carried out to examine the flow and temperature fields as well as heat transfer rates in a constant wall temperature cavity resembling the laser produced cavity situation. An impinging gas normal to the cavity surface is considered while cavity wall temperatures are set at elevated temperature similar to the melting temperature of the substrate material. RSTM is employed to account for the turbulence behavior of the flow. The flow and temperature fields are obtained numerically using a control-volume approach. The study is extended to include the various depths of the cavity. Air is used as impinging gas while steel is used as workpiece material.

## Turbulence model

The governing flow and energy equations for the axisymmetric impinging jet may be written in the Cartesian tensor notation as:

The continuity equation is:

$$\frac{\partial}{\partial x_i}(\rho U_i) = 0 \tag{1}$$

The momentum equation is:

$$\frac{\partial}{\partial x_i}(\rho U_i U_j) = -\frac{\partial p}{\partial x_j} + \frac{\partial}{\partial x_i}\left[\mu\left(\frac{\partial U_i}{\partial x_j} + \frac{\partial U_j}{\partial x_i}\right) - \rho R_{ij}\right] \tag{2}$$

The energy equation is:

$$\frac{\partial}{\partial x_i}(\rho U_i h) = \frac{\partial}{\partial x_i}\left[\frac{\mu}{\sigma}\frac{\partial h}{\partial x_i} - \rho R_{ih}\right] \tag{3}$$

when modelling the Reynolds stresses and turbulence properties the following steps are considered.

Reynolds Stresses ($R_{ij}$):

The RSTM is based on the second-moment closure (Launder and Rodi, 1983; Craft, 1991). The transport equation of the Reynolds stress ($R_{ij}$) is:

$$\frac{\partial}{\partial x_m}(U_m R_{ij}) = P_{ij} + \Lambda_{ij} - \epsilon_{ij} + \Pi_{ij} + \Pi_{ij}^{w} \tag{4}$$

where $P$, $\Lambda$, $\epsilon$, $\Pi$ and $\Pi^{w}$ are the rate of production, transport by diffusion, rate of dissipation, transport due to turbulent pressure excluding strain interactions

and transport due to wall reflection respectively. Equation (4) consists of six partial differential equations; one for the transport of each of the six independent Reynolds stresses. The production term ($P_{ij}$), diffusion ($\Lambda_{ij}$), dissipation ($\epsilon_{ij}$), transport due to turbulent pressure ($\Pi_{ij}$) and the wall reflection ($\Pi^{w}_{ij}$) terms may be written as:

Production term:

$$P_{ij} = -\left(R_{im}\frac{\partial U_j}{\partial x_m} + R_{jm}\frac{\partial U_i}{\partial x_m}\right) \tag{5}$$

Diffusion term:

$$\Lambda_{ij} = \frac{\partial}{\partial x_m}\left(\frac{\nu_t}{\sigma_k}\frac{\partial R_{ij}}{\partial x_m}\right) \tag{6}$$

with

$$\nu_t = C_\mu \frac{k^2}{\epsilon}; \quad C_\mu = 0.09 \quad \text{and} \quad \sigma_k = 1.0 \tag{7}$$

Dissipation rate:

$$\epsilon_{ij} = \frac{2}{3}\epsilon\delta_{ij} \tag{8}$$

where $\epsilon$ is the dissipation rate of turbulent kinetic energy defined earlier and $\delta_{ij}$ is the Kronecker delta.

Transport due to turbulent pressure:

$$\Pi_{ij} = \Pi_{ij1} + \Pi_{ij2} = -C_1\frac{\epsilon}{k}\left(R_{ij} - \frac{2}{3}k\delta_{ij}\right) - C_2\left(P_{ij} - \frac{2}{3}p\delta_{ij}\right) \tag{9}$$

with $C_1 = 1.8$ and $C_2 = 0.6$.

The wall reflection term (Craft, 1991):

$$\Pi^{w}_{ij} = \left[C_{1w}\frac{\epsilon}{k}\begin{pmatrix} R_{ml}n_m n_l\delta_{ij} \\ -\frac{3}{2}R_{im}n_m n_j \\ -\frac{3}{2}R_{jm}n_m n_i \end{pmatrix} + C_{2w}\begin{pmatrix} \Pi_{ml2}n_m n_l\delta_{ij} \\ -\frac{3}{2}\Pi_{im2}n_m n_j \\ -\frac{3}{2}\Pi_{jm2}n_m n_i \end{pmatrix}\right]\frac{k^{3/2}}{C_l\epsilon z} \tag{10}$$

where $n$ is the normal vector, $C_{1w} = 0.5$, $C_{2w} = 0.3$, and $C_l = 2.5$.

The turbulent kinetic energy ($k$) is $k = \frac{1}{2}(R_{11} + R_{22} + R_{33})$, where $R_{11}$, $R_{22}$ and $R_{33}$ are the normal stresses.

The transport equation for energy dissipation rate ($\epsilon$) is:

$$\frac{\partial}{\partial x_i}(\rho U_i\epsilon) = C_\epsilon\frac{\partial}{\partial x_i}\left[\frac{R_{ij}}{\epsilon}k\frac{\partial\epsilon}{\partial x_i}\right] + C_{1\epsilon}\frac{1}{2}\frac{\epsilon}{k}E_{ij}.E_{ij} - C_{2\epsilon}\frac{\epsilon^2}{k} \tag{11}$$

The six equations for Reynolds stress transport are solved along with a model equation for the scalar dissipation.

Turbulent heat transport is modelled using the concept of Reynolds analogy to turbulent momentum transfer, i.e.

$$-\rho R_{ih} = \frac{\mu_t}{\sigma_h}\frac{\partial h}{\partial x_i}$$

where

$$\mu_t = \rho C_\mu \frac{k^2}{\epsilon}$$

*1.1 Heat conduction equation*

The heat conduction in a stationary medium can be formulated using the Fourier heating model. Therefore, the equation governing the heat conduction yields a modified form of equation (3), i.e.:

$$K\frac{\partial}{\partial x_i}\left[\frac{\partial T}{\partial x_i}\right] = 0 \tag{12}$$

where $K$ is the thermal conductivity of solid, which is steel.

*1.2 Flow boundary conditions*

Four boundary conditions are considered, these are:

*Solid wall:* No slip condition is assumed at the solid wall and the boundary condition for the velocity at the solid wall is therefore:

$$U_i = 0$$

*Generalized wall functions for normal and shear turbulent stresses for the RSTM models:* When the flow is very near the wall it undergoes a rapid change in direction, the wall-functions approach is not successful in reproducing the details of the flow. Consequently, the turbulent stresses and fluxes at the near wall grid points are calculated directly from their transport equations. In this case, the near-wall region lying between the wall and the near-wall computational node at $x_\mathrm{p}$ can be represented by two layers: the fully viscous sublayer, defined by $\mathrm{Re}_v = x_v\sqrt{k_v}/\nu \cong 20$, and a fully-turbulent layer. Based on the assumption that local equilibrium prevails in the turbulent layer, i.e. production equals dissipation for the turbulent kinetic energy, the above results,

$$\frac{U_\mathrm{p}}{\tau_w/\rho}C_\mu^{\frac{1}{4}}\sqrt{k_\mathrm{p}} = \frac{1}{\kappa}\ln\left(\chi x_\mathrm{p}\frac{C_\mu^{\frac{1}{4}}\sqrt{k_\mathrm{p}}}{\nu}\right) \tag{13}$$

which yields the wall shear stress near the wall i.e. $\overline{vw}|_{z_v} = \tau_w/\rho$, which serves as the boundary condition for the $\overline{vw}$ transport equation.

In relation to normal stresses, the turbulence energy must decrease quadratically towards a value of zero (Benocci, 1991) at the wall, therefore a zero-gradient condition for the normal stresses is physically realistic. This situation is insufficient to ensure an accurate numerical representation of near-wall effects. An improved approach for internal cells is needed in respect of evaluating volume-integrated production and dissipation of normal stresses (these are normally evaluated at cell centers, using linear interpolation, and then multiplied by the cell volume). Considering $\overline{v^2}$ as an example, the volume-integrated production of $\overline{v^2}$ between the wall and the $P$-node may be approximated by Hogg and Leschziner (1989),

$$\int_{\Delta r}\int_{0}^{z_p} P_{22}\,\mathrm{d}\forall \cong \int_{\Delta r}\int_{z_v}^{z_p} -2\overline{vw}\frac{\partial V}{\partial x}\,\mathrm{d}\forall = 2\tau_w\left(\frac{V_p - V_v}{x_p - x_v}\right)x_p\Delta r \qquad (14)$$

where $V_p$ and $V_v$ follow from the log-law, equation (13). No contribution arises from the viscous sublayer since $\overline{vw} = 0$ in this layer. An analogous integration of the dissipation rate with the assumptions,

$$\epsilon = \frac{2\nu k_v}{x_v^2} \qquad 0 \le x \le x_v$$

$$\epsilon = \frac{C_\mu^{3/4} k_p^{3/2}}{\kappa x_v} \qquad x_v \le x < x_p$$

leads to

$$\int_{\Delta r}\int_{0}^{x_p} \epsilon\,\mathrm{d}\forall \cong \left[\frac{2\nu k_p}{x_v} + \frac{C_\mu^{3/4} k_p^{3/2}}{\kappa}\ln\left(\frac{x_p}{x_v}\right)\right]\Delta r \qquad (15)$$

an analogous treatment is applied to $\overline{v^2}$, while the production of $\overline{w^2}$ in the viscous and turbulent near wall layers region is zero (Versteeg and Malalasekera, 1995).

The values resulting from equations (14) and (15) are added, respectively, to the volume-integrated generation and dissipation computed for the upper half of the near-wall volume.

It should be noted that for the wall-law approach, the near-wall dissipation ($\epsilon_p$) is not determined from its differential equation applied to the near-wall cell surrounding the node. Instead, and in accordance with the log-law, this value is obtained via the length scale from

$$\epsilon_p = \frac{C_\mu^{3/4} k_p^{3/2}}{\kappa z_p},$$

which serves as the boundary conditions for inner cells.

*Inlet conditions:* The boundary conditions for temperature and velocity need to be introduced:

$$T = \text{specified } (300\,\text{K}) \text{ and } U = \text{specified } (100\,\text{m/s})$$

The values of $k$ and $\epsilon$ are not known at the inlet, but can be determined from turbulent kinetic energy i.e.:

$$k = \lambda \bar{u}^2 \tag{16}$$

where $\bar{u}$ is the average inlet velocity and $\lambda$ is a percentage.

The dissipation is calculated from:

$$\epsilon = C_\mu \frac{k^{\frac{3}{2}}}{aD},$$

where $D$ is the diameter. The values $\lambda = 0.03$ and $a = 0.005$ are commonly used and may vary slightly in the literature (Bradshaw *et al.*, 1981).

*Outlet:* The flow is considered to be extended over a long domain, therefore, the boundary condition (unbounded boundaries – Figure 1) for any variable $\phi$ is:

$$\frac{\partial \phi}{\partial x_i} = 0 \tag{17}$$

where $x_i$ is the normal direction at outlet.

*Symmetry axis:* At the symmetry axis, the radial derivative of the variables is set to zero, i.e.:

$$\frac{\partial \phi}{\partial r} = 0 \tag{18}$$

except

$$V = \overline{vw} = \overline{vh} = \overline{wh} = 0$$

*1.2.1 Solid side. Convection boundary:* Convection with a constant coefficient for still air ($h = 5\,\text{W/m}^2\,\text{K}$) is considered at the $x = x_{\max}$ boundary for the plate (boundary A in Figure 1).

*Constant temperature boundary:* Two constant temperature boundaries are considered. First one is in the radial direction far away from the symmetry axis constant temperature $T = T_{\text{amb}}$ (300 K) is defined (boundary B in Figure 1). It should be noted that the constant temperature boundary condition was set at different locations in the radial directions and no significant effect of T=constant, was observed on the temperature and flow field in the stagnation region. Therefore, this boundary condition is set for radial distance 0.010 m from the symmetry axis. The second constant temperature boundary is set at cavity walls (as shown in Figure 1) $T = 1,500\,\text{K}$.

*1.2.2 Solid fluid interface.* The coupling of conduction within the solid and convection within the fluid, termed conjugation, is required for the present

analysis at the solid fluid interface. The appropriate boundary conditions are continuity of heat flux and temperature and are termed boundary conditions of the fourth kind. i.e.:

$$T_{w_{\text{solid}}} = T_{w_{\text{gas}}}$$

$$K_{w_{\text{solid}}} \frac{\partial T_{w_{\text{solid}}}}{\partial x} = K_{w_{\text{gas}}} \frac{\partial T_{w_{\text{gas}}}}{\partial x}$$

No radiation losses from the solid surface is assumed.

*1.3 Gas and solid properties*

The equation of state is used for air and constant properties are employed for steel. The properties employed are given in Table I.

## Numerical method and simulation

A control volume approach is employed when discretizing the governing equations. The discretization procedure is given in (Patankar, 1980). The problem of determining the pressure and satisfying continuity may be overcome by adjusting the pressure field so as to satisfy continuity. A staggered grid arrangement is used in which the velocities are stored at a location midway between the grid points, i.e. on the control volume faces. All other variables including pressure are calculated at the grid points. This arrangement gives a convenient way of handling the pressure linkages through the continuity equation and is known as Semi-Implicit Method for Pressure-Linked Equations (SIMPLE) algorithm. The details of this algorithm is given in (Patankar, 1980).

The schematic view of the impinging jet and the cavity is shown in Figure 1a while the grid generated in the present simulation is shown in Figure 1b. Figure 2 shows the grid independent test results. The grid-independent tests are carried out by considering $40 \times 33$, $45 \times 35$, $70 \times 55$, $90 \times 70$, and $110 \times 90$ grid points. The number of grid points resulting grid independency are $90 \times 70$ in the $x$ and $r$ plane, respectively.

## 2. Results and discussions

Gas jet impinging onto a cylindrical cavity is considered to resemble the edges generated during laser cutting process. The edges of the cavity are assumed at elevated temperature (the melting temperature of the substrate material $\sim$1,500 K) and remain at this temperature during the simulation; consequently, constant temperature source is assumed at walls of the cavity. The impinging gas, which is air, has properties, which are governed by the equation of state. The height of the cavity is varied at four levels, which is given in Table II.

In order to account for the turbulence effects RSTM is employed in the analysis. The governing equations of flow and energy are solved numerically using a control-volume approach.

Figures 3-5 show the product of fluctuating velocities (turbulence stresses) along the symmetry axis for different cavity depths. In the case of a flat plate (zero cavity height), near the stagnation point, the present simulation predicts slightly high level of turbulent fluctuations, which is consistent with the early work (Shuja *et al.*, 2001). Once the cavity is introduced, the turbulence fluctuations moves towards the cavity with increased magnitude. This occurs because of the stagnation point which moves inside the cavity as well as high spreading rate in this region; consequently, these, in turn, increase the turbulence intensity. Moreover, this situation also increases the shear stress levels which can be observed from Figure 3, in which $u'v'/u_0^2$ variation along the symmetry axis is shown. Moreover, turbulent properties dies in the cavity beyond the stagnation point as depth increases. In the case of shallow cavity (0.2 mm depth), mixing of the fluid enhances the turbulent levels in the stagnation region, which in turn results in high magnitude of turbulence shear stresses. The peak value of $u'v'/u_0^2$ indicates that jet extends into the cavity with increasing depth. Moreover, the ratio of jet penetration is not as high as the ratio expansion of the cavity depth. The high magnitude of turbulence fluctuations is affected by the gas temperature due to corresponding gas thermodynamic pressure in the cavity, since the fluid properties vary with temperature.

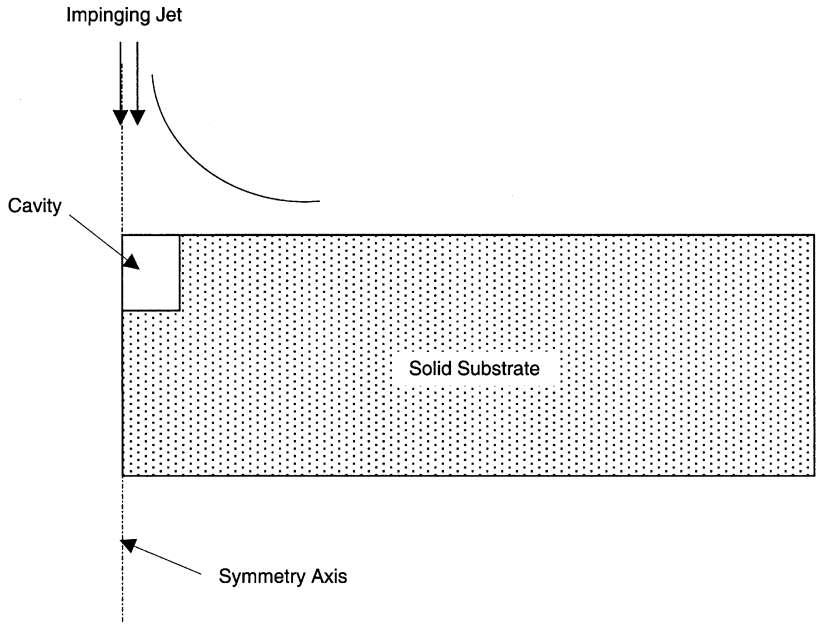


**Figure 1.**
(a) Schematic view of the impinging jet and the cavity, (b) The solution domain with the computation grid

*(continued)*

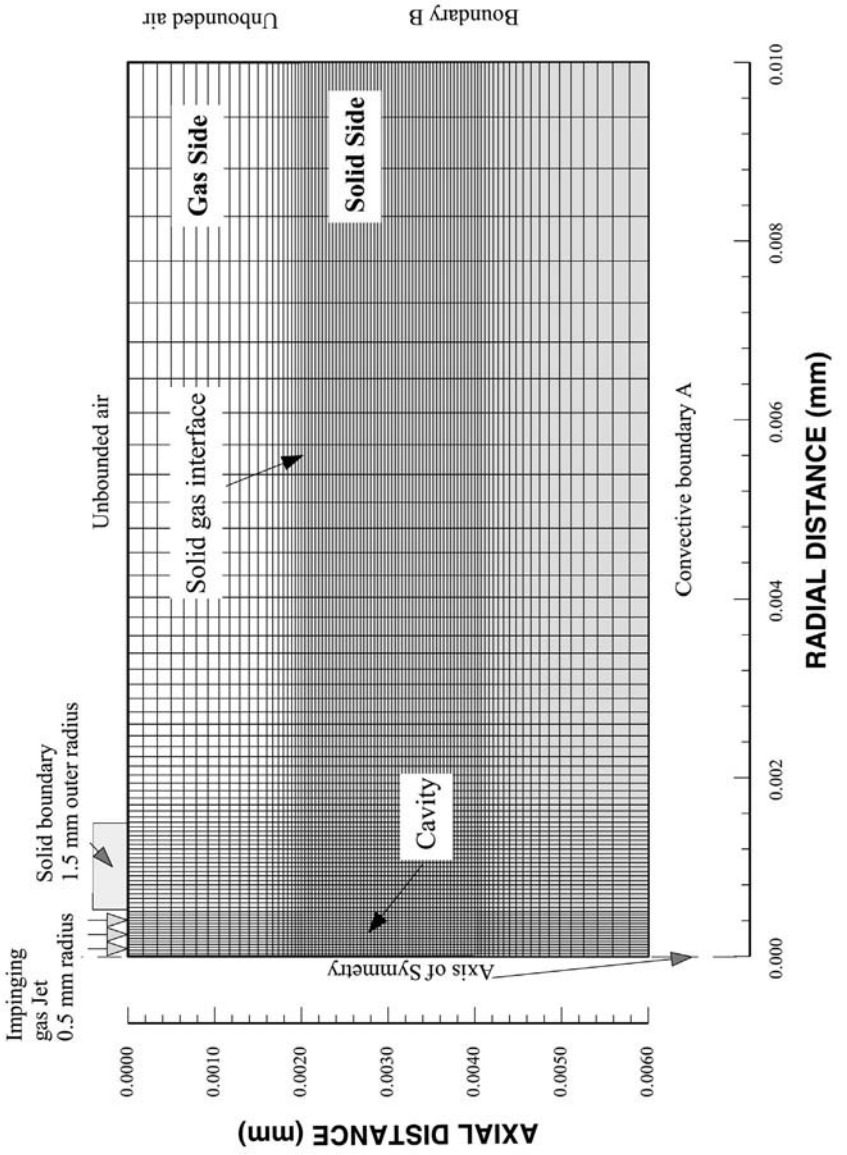
Unbounded air
Boundary B
Gas Side
Solid Side
Solid gas interface
Unbounded air
Solid boundary
1.5 mm outer radius
Impinging
gas Jet
0.5 mm radius
Cavity
Axis of Symmetry
Convective boundary A
AXIAL DISTANCE (mm)
0.0000
0.0010
0.0020
0.0030
0.0040
0.0050
0.0060
RADIAL DISTANCE (mm)
0.000
0.002
0.004
0.006
0.008
0.010
(b)

**Figure 1.**

Figure 6 shows the flow and temperature fields in whole solution domain. The far field of the flow is not affected by the presence of the wall. However, temperature field in the solid side changes as the depth of the cavity varies. In this case, high temperature region extends further around the cavity as the depth increases. This is, mainly, because of the extended length of the constant temperature boundary, since increasing the depth of the cavity increases the

| Property | | Gas (Air) | Solid (Steel) |
|---|---|---|---|
| Density | $\rho$ (kg/m$^3$ | $p/RT$ | 8030 |
| Thermal conductivity | $K$ (W/m K) | 0.0242 | 16.27 |
| Specific heat capacity | $c_p$ (J/kg K) | 1006.43 | 502.48 |
| Viscosity | $\nu$ (m$^2$/s) | $1.7894\times10^{-5}$ | |

**Table I.**
Properties used in the simulation

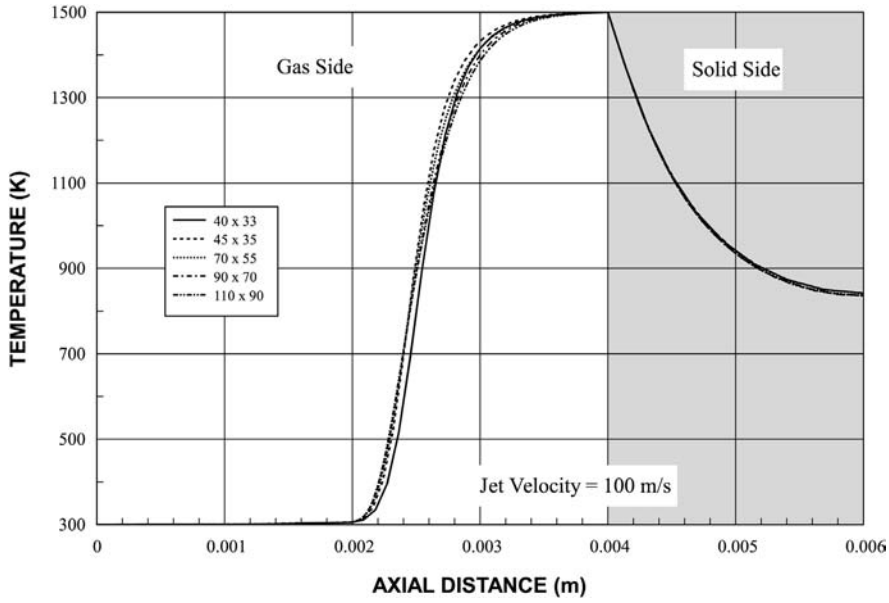


**Figure 2.**
The results of grid independence tests along the symmetry axis

| Cases | Depth of cavity (mm) |
|---|---|
| 1 | 0.0 |
| 2 | 0.2 |
| 3 | 0.5 |
| 4 | 1.0 |
| 5 | 2.0 |

**Table II.**
Cavity depths for different cases

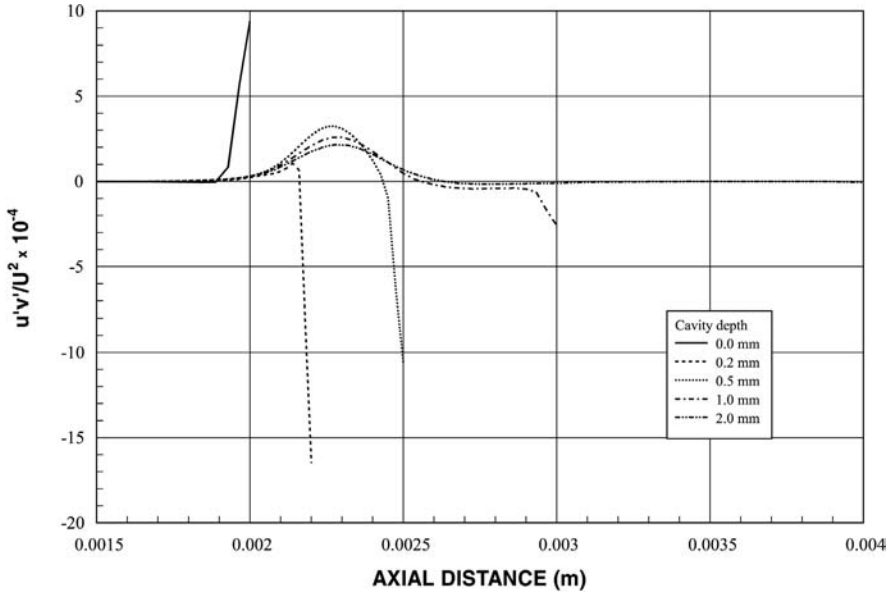


**Figure 3.**
Variation of normalized turbulent Reynold's stress along the symmetry axis

length of the side wall where constant temperature source is inputted. Moreover, some small circulation cell is developed next to the jet boundary. The orientation of circulation cell is not influenced by the cavity depth and the influence of the cell on the temperature field is negligible.

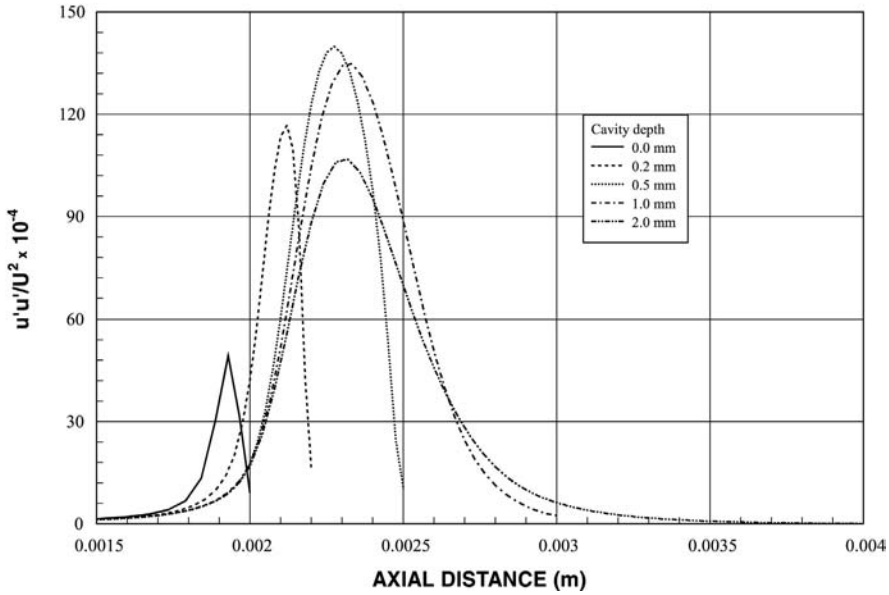


**Figure 4.**
Variation of normalized turbulent Reynold's stress along the symmetry axis

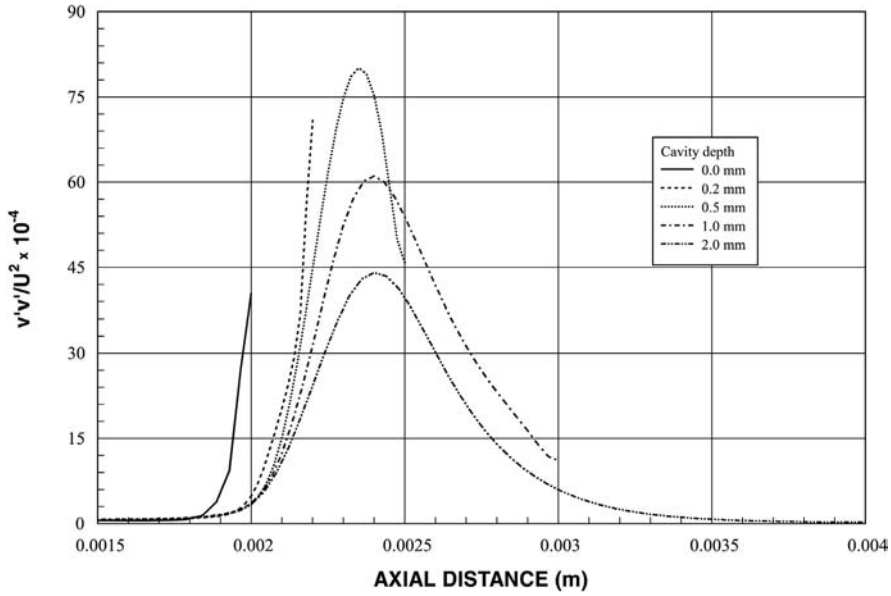


**Figure 5.**
Variation of normalized turbulent Reynold's stress along the symmetry axis

Figure 7 shows the velocity vectors and resulting temperature contours in and around the cavity provided that temperature contours and velocity vectors in the first figure correspond to zero cavity height (flat plate). In the flat plate case (where the cavity depth is zero), the fluid temperature away from the solid wall is not influenced by the wall temperature provided that in the surface vicinity of the wall, fluid temperature is affected considerably due to convective heating. Since, the flow parameters in the surface region are not plotted in the figure, this influence could not be observed explicitly. In the case of a small cavity depth (0.2 mm), boundary-layer-like flow develops, however, as the distance from the symmetry axis increases towards the cavity wall, the boundary-layer-like flow becomes thinner. In this case, the upstream flow, with high velocity, above the surface influences the flow in the cavity. This influence becomes less in the region close to the cavity side wall. The gas temperature in the cavity increases, but temperature above the surface becomes almost identical to those corresponding to a flat plate case. As the cavity depth increases, the flow in the cavity decelerates, i.e. the boundary-layer-like flow becomes thinner close to the side wall. This occurs because of the fluid in the cavity is heated and its pressure rises according to the equation of state. This is more pronounced close to the walls. As the cavity depth increases, the thermodynamic pressure build up partially blocks the upstream flow entering the cavity. In addition, the static pressure developed in the vicinity of the walls also has similar effects on the flow entering the cavity. Consequently, the static and thermodynamic pressure fields result in negative velocity gradient in the

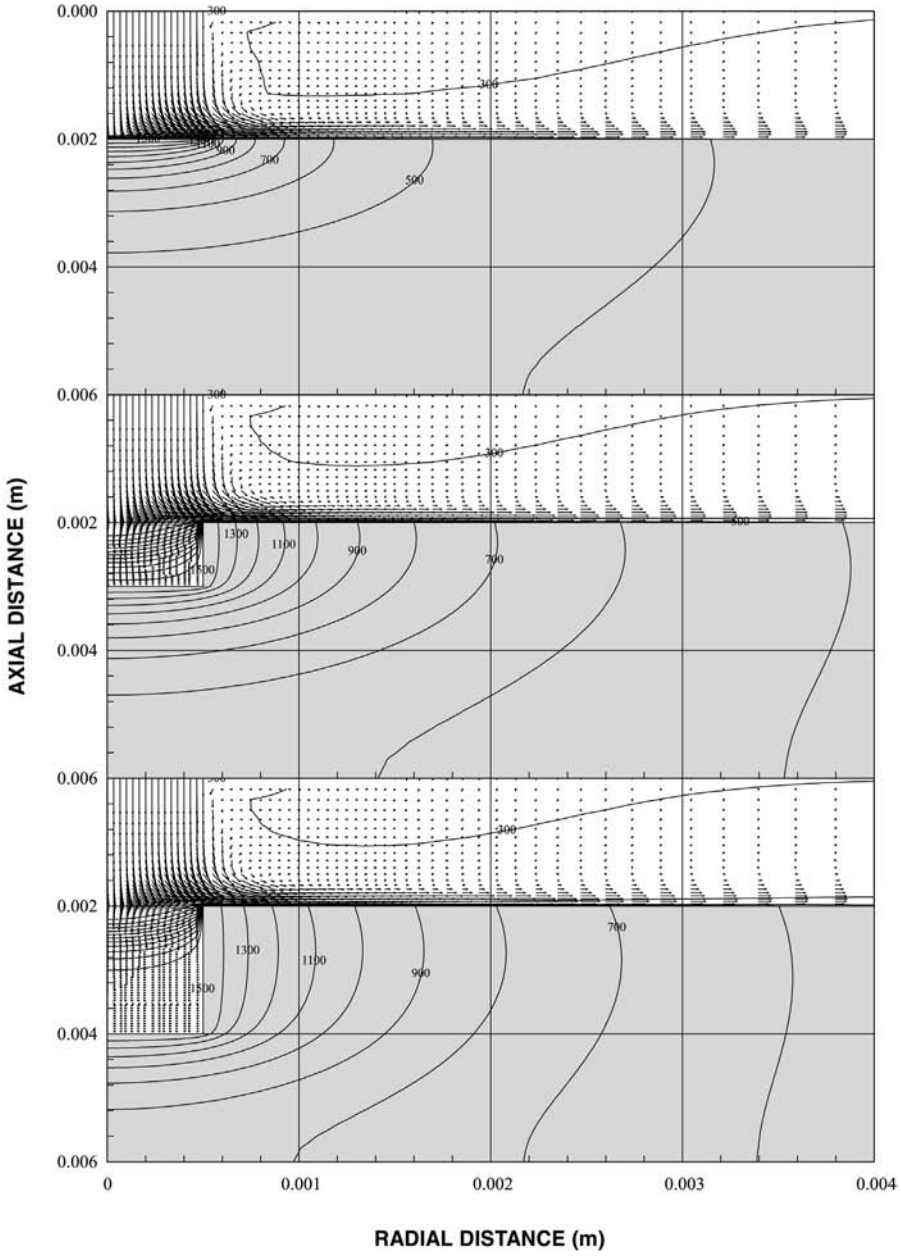


**Figure 6.**
Velocity vectors and temperature contours in solid and gas sides

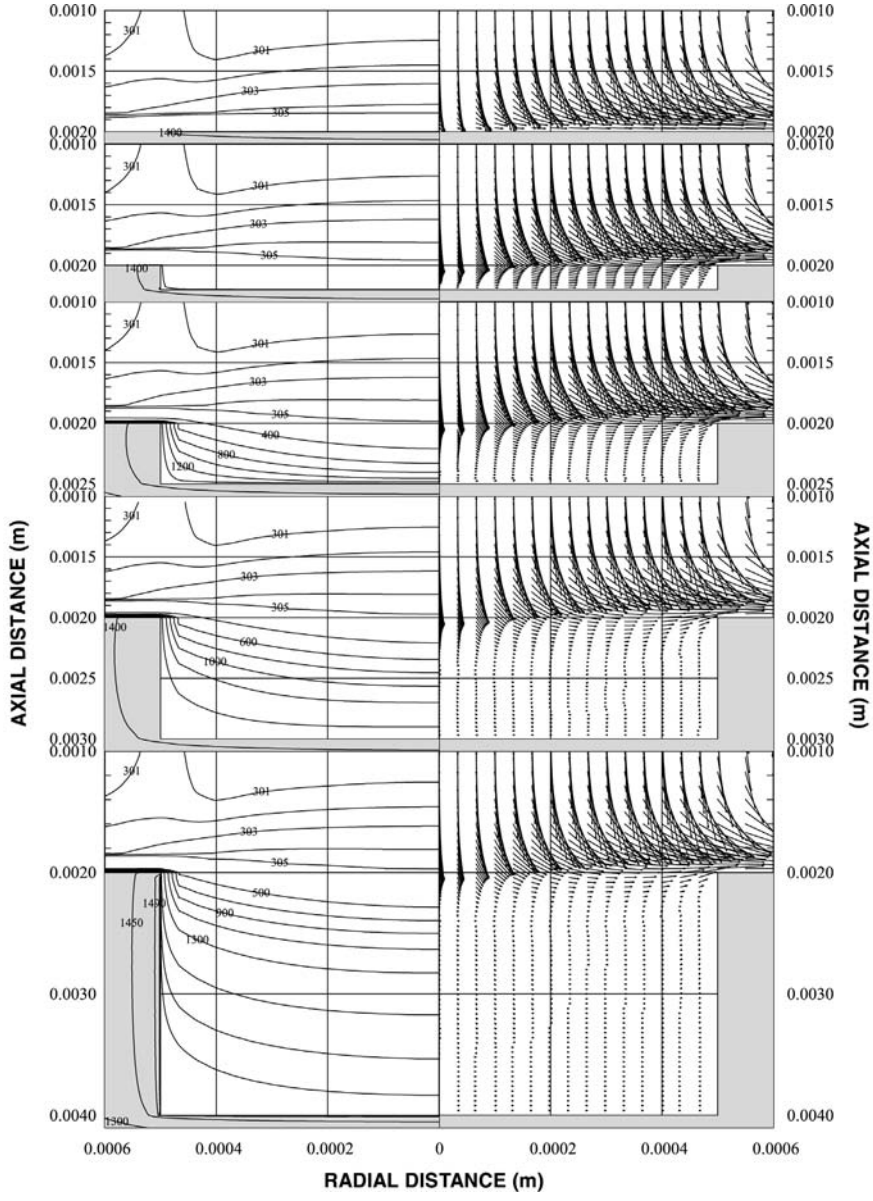


**Figure 7.**
Velocity vectors and temperature contours in and around the cavity

boundary-layer-like flow in the region close to the walls. The temperature rise can be seen from the temperature contours, i.e. temperature attains considerably high values in the region close to the walls. At the cavity depth of 1 mm and more, the reverse flow occurs in the cavity. In this case, flow develops from a heated wall and dies towards the symmetry axis.

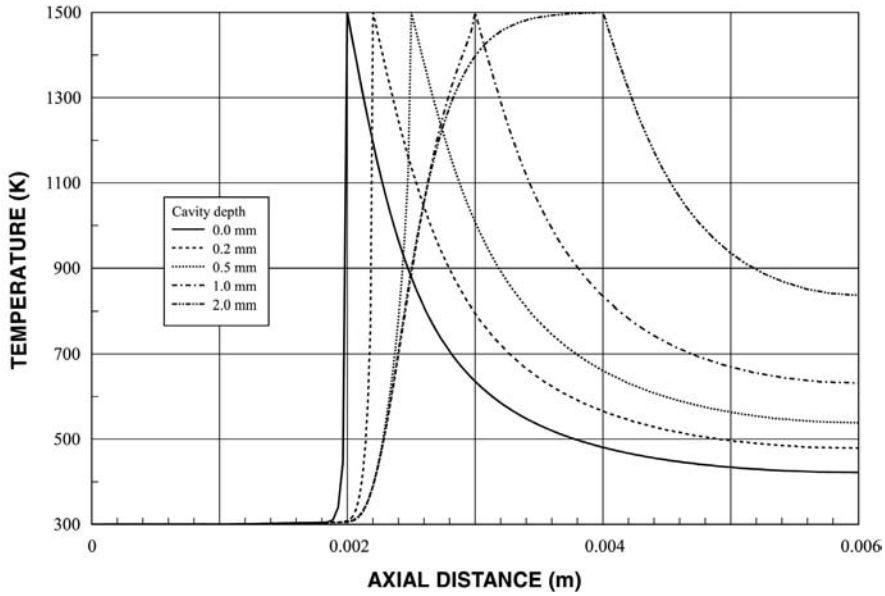


**Figure 8.**
Temperature profiles along the symmetry axis in the gas and solid sides

Figure 8 shows the temperature profiles along the symmetry axis in the whole field including gas and solid sides. Temperature changes sharply in the gas side for a flat plate case, since the wall temperature is at elevated temperature. Consequently, the thickness of the thermal boundary layer is considerably small due to high jet velocity, which, in turn, results in high radial velocity close to the wall as consistent with the early work (Shuja *et al.*, 1998). In the case of a shallow cavity, temperature profiles behave almost similar to that corresponding to a flat plate case, provided that gas temperature in the cavity attains high values while it reduces sharply in the region of the symmetry axis. This is because of the impinging gas jet effect, in which case, impinging gas with high momentum purges the gas in the cavity developing a radial flow as seen from Figure 7. Consequently, cool gas replaces with the heated gas in the region of the symmetry axis in the cavity. As the cavity depth increases further, gas temperature in the cavity increases and close to the wall sharp change in temperature occurs. The gradual increase in temperature across the cavity width, except close to the side wall, is due to impinging gas jet effect. In this case, impinging gas develops a flow in the cavity, which in turn enhances the convective heat transfer from the walls. The sharp change in temperature in the region close to the walls is because of high wall temperature and low flow velocity in this region, i.e. high thermodynamic pressure is built up in this region. Consequently, high pressure retards the incoming flow towards the walls and in some cases (for large cavity depths) reverse flow emanating from walls is developed in the cavity due to high thermodynamic pressure.

Figure 9a shows the logarithmic plot of the Nusselt number variation along the bottom wall of the cavity. The Nusselt number remains almost constant along the width of the wall with the exception that small decrease in the Nusselt number occurs in the region close to the side wall. This is because of the high wall temperature which generates a high thermodynamic pressure in this region. Consequently, flow retards and heat transfer rates from the bottom wall reduces. Moreover, as the depth increases, the Nusselt number reduces. This is again due to low flow velocity development because of high pressure generated in the cavity. As the depth increases further, the Nusselt number reduces drastically. This occurs because of the reverse flow developed in the cavity. Moreover, the Nusselt number reduces further towards the side wall in the cavity. Figure 9b shows the Nusselt number variation along a side wall of the cavity. The Nusselt number increases from the edge of the cavity surface towards some depth below the surface and it reaches its maximum before it decays with increasing distance along the side wall towards the bottom of the cavity. The attainment of the maximum Nusselt number at some depth below the cavity surface is because of the high rate of convective cooling, i.e. velocity attains high values in this region for all depths. Moreover, the Nusselt number decreases sharply along the side wall for shallow cavities (cavity depth $\leq 0.5$ mm). This occurs because of the temperature field generated in the cavity, i.e. high temperature gas close to the wall generates high thermodynamic pressure in this region. Since the reverse flow emanating from the side wall is suppressed by the jet, a stagnation occurs in the region close to the wall. This, in turn, results in low heat transfer rates and, therefore, the Nusselt number decreases sharply along the wall. In case of large depths, the Nusselt number decays gradually as the distance along the side wall towards the bottom of the cavity increases. This is because of the fact that as the depth increases, the influence of gas jet on the flow field reduces in the cavity.

Figure 10 shows the pressure coefficient ($2\Delta P/\rho V_j^2$) along the symmetry axis in the cavity. The sharp increase in the pressure coefficient represents the stagnation region in the cavity due to impinging jet. The pressure maxima moves towards the bottom of the cavity as depth increases, provided the ratio of this movement is very small as compared to the ratio of increase in the depth. This indicates the extension of impinging jet into the cavity. The pressure coefficient further increases beyond the stagnation point. This increase is related to the thermodynamic pressure rise due to the high temperature of the fluid in the cavity. Moreover, the pressure coefficient reduces to minimum before increases and attains a steady value for large depths. The decrease in the pressure coefficient behind the stagnation region is due to flow developed in this region. The high pressure region in the cavity extends almost 2/3 of the depth.

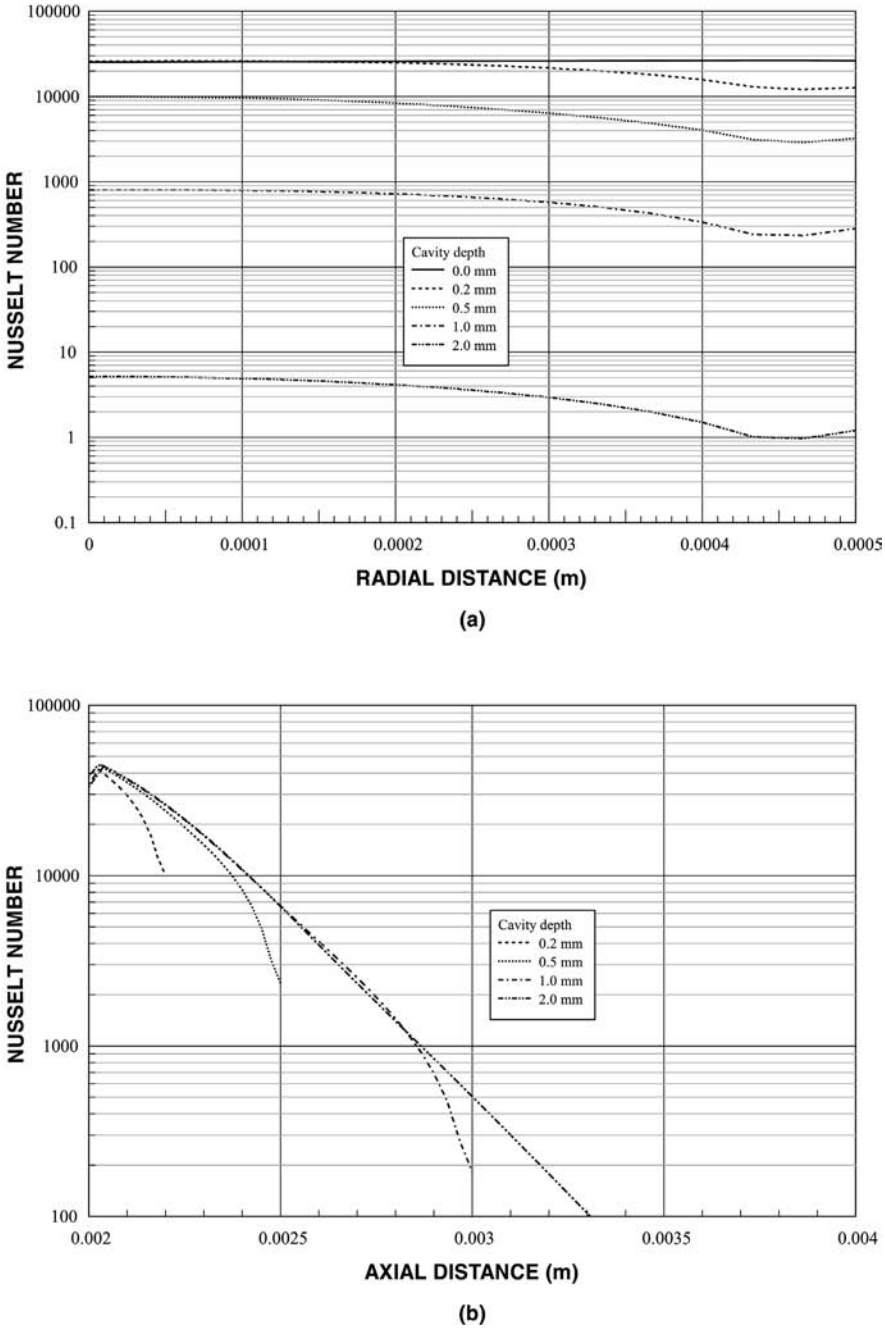


**Figure 9.**
(a) The Nusselt number variation along the bottom surface of the cavity, (b) The Nusselt number variation along the side wall of the cavity

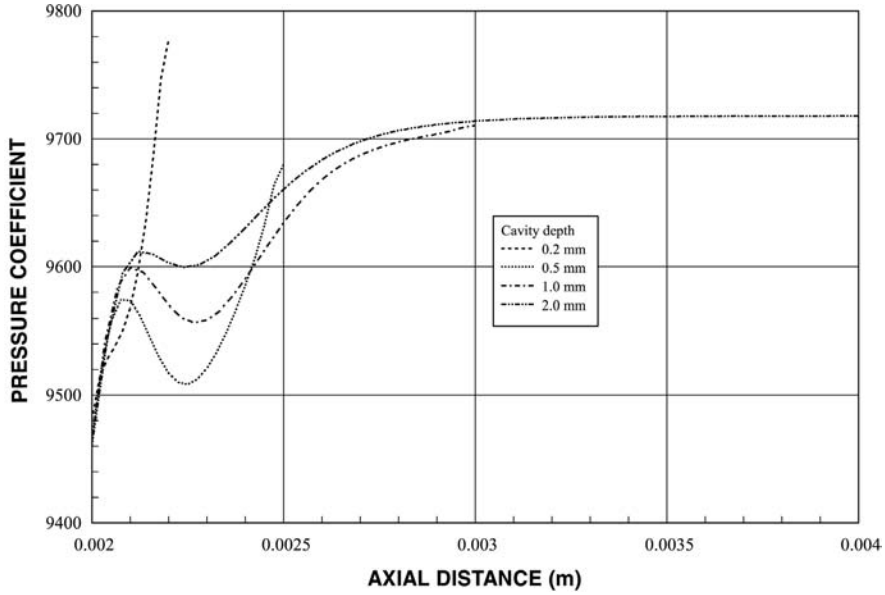


**Figure 10.**
Pressure coefficient along the symmetry axis inside the cavity

## Conclusions

The gas-jet impingement onto a cylindrical cavity resembling almost the laser-generated shroud cavity is considered. The cavity walls are assumed to be at an elevated temperature similar to the melting temperature of the substrate material. The flow and temperature fields are computed numerically using a control volume approach for different cavity depths. In order to account for the turbulence effects of the impinging jet, the RSTM is employed. It is found that jet extends further into the cavity with increasing depth; however, the ratio of jet extension is not as high as the ratio of expansion of the cavity depth. The Nusselt number across the side wall is influenced considerably by the depth while the Nusselt number remains almost constant at the bottom surface of the cavity. A high temperature region develops a high thermodynamic pressure, which in turn generates a flow emanating from the side wall towards the symmetry axis, provided that the mean flow velocity is considerably small. The specific conclusions derived from the present study can be listed as follows.

(1) Temperature field above the plate surface does not alter significantly with the depth of the cavity while high temperature field extends further inside the solid side as the depth increases. Temperature rise in the vicinity of the cavity walls generates high thermodynamic pressure field, which in turn retards the flow diffusing from symmetry axis towards the cavity wall.

(2) The Nusselt number reduces in the region along the bottom wall. In this case, reverse flow generated from the side wall mixes with the flow in the cavity due to jet impingement, which results in stagnation region in the bottom corner of the cavity. This, consequently, reduces the heat transfer rates and lowers the Nusselt number. In the case of a side wall, reverse flow increases heat transfer rates and the Nusselt number increases considerably, provided that increasing depth reduces the Nusselt number along the side wall. Moreover, the Nusselt number increases to its maximum at some depth below the cavity surface. This is because of the enhanced heat transfer rates in this region.

(3) Stagnation region moves into the cavity with increasing depth. Pressure increases along the symmetry axis as the depth increases. Moreover, as depth increases further a high pressure region is developed in the cavity due to enhancement of thermodynamic pressure.

## References

Aloke, R., Girish, V., Scrutton, R.F. and Molian, P.A. (1997), "A model for prediction of dimensional tolerances of laser of cut holes in mild steel thin plates", *International Journal of Machine Tools and Manufacturing*, Vol. 37 No. 8, pp. 1069-78.

Baughn, J.W. and Shimizu, S. (1989), "Heat transfer measurements from a surface with uniform heat flux and an impinging jet", *ASME Journal of Heat Transfer*, Vol. 111, pp. 1096-8.

Benocci, C. (1991), *Introduction to the modeling of turbulence, 1991–02*, Von Karman Institute for Fluid Dynamics.

Bradshaw, P., Cebeci, T. and Whitelaw, J.H. (1981), *Engineering Calculation Methods for Turbulent Flow*, chapter 3. Academic press, New York, p. 51.

Chen, S.L. (1998), "The effects of gas composition on the $co_2$ laser cutting of mild steel", *Journal of Material Processing Technology*, Vol. 73, pp. 147-59.

Craft, T.J. (1991), "Second-moment modeling of turbulent scalar transport", PhD thesis, Faculty of Technology, University of Manchester.

Gonsalves, J.N. and Duley, W.W. (1972), "Cutting thin metal sheets with the cw $CO_2$ laser", *Journal of Applied Physics*, Vol. 43 No. 11, pp. 4684-7.

Hogg, S. and Leschziner, M.A. (1989), "Second-moment-closure calculation of strongly swirling confined flow with large density gradients", *International Journal of Heat and Fluid Flow*, Vol. 10 No. 1, pp. 16-27.

Hosseinalipour, S.M. and Mujumdar, A.S. (1995), "Comparative evaluation of different turbulence models for confined impinging and opposing jet flows", *Numerical Heat Transfer, Part A*, Vol. 28, pp. 647-66.

Jambunathan, K., Lai, E., Moss, M.A. and Button, B.L. (1992), "A review of heat transfer data for single circular jet impingement", *International Journal of Heat and Fluid Flow*, Vol. 13, pp. 106-15.

Kar, A., Rothenflue, J.A. and Latham, W.P. (1997), "Scaling laws for thick-section cutting with a chemical oxygen-iodine laser", *Journal of Laser Applications*, Vol. 9, pp. 279-86.

Lasher, W.C. and Taulbee, D.B. (1994), "Reynolds stress model assessment using round jet experimental data", *International Journal of Heat and Fluid Flow*, Vol. 15 No. 5, pp. 357-63.

Launder, B.E. and Rodi, W. (1983), "The turbulent wall jet – measurement and modeling", *Annual Review of Fluid Mechanics*, Vol. 15, pp. 429-33.

Morris, G.K., Garimella, S.V. and Amano, R.S. (1996), "Prediction of jet impingement heat transfer using a hybrid wall treatment with different turbulent Prandtl number functions", *ASME Journal of Heat Transfer*, Vol. 118, pp. 562-9.

Patankar, S.V. (1980), *Numerical Heat Transfer*, McGraw-Hill, New York.

Patel, V.C., Rodi, W. and Scheuerer, G. (1985), "Turbulence models for near-wall and low Reynolds number flows: review", *AIAA Journal*, Vol. 23 No. 9, pp. 1308-19.

Prasad, G.V.S., Siores, E. and Wong, W.C.K. (1998), "Laser cutting of metallic coated sheet steels", *Journal of Materials Processing Technology*, Vol. 74, pp. 234-42.

Sheng, P. and Chryssolouris, G. (1994), "Investigation of acoustic sensing for laser machining processes, part 2: laser grooving and cutting", *Journal of Material Processing Technology*, Vol. 43, pp. 145-63.

Shuja, S.Z. and Yilbas, B.S. (2000), "The influence of gas jet velocity in laser heating – a moving workpiece case", *Proceeding of the Institute of Mechanical Engineers, Part C*, Vol. 214, pp. 1059-78.

Shuja, S.Z., Yilbas, B.S. and Budair, M.O. (1998), "Modeling of laser heating of solid substance including assisting gas impingement", *Numerical Heat Transfer, Part A*, Vol. 33, pp. 315-39.

Shuja, S.Z., Yilbas, B.S. and Budair, M.O. (2001), "Local entropy generation in an impinging jet: Minimum entropy concept evaluating various turbulence models", *Computer Methods in Applied Mechanics and Engineering*, Vol. 190, pp. 3623-44.

Strahle, W.C., Sigman, R.K. and Meyer, W.L. (1987), "Stagnation turbulent flows", *AIAA Journal*, Vol. 25 No. 8, pp. 1071-7.

Versteeg, H.K. and Malalasekera, W. (1995), *An Introduction to Computational Fluid Dynamics, The Finite Volume Method*, Longman Scientific and Technical.

Yilbas, B.S. (1997), "The analysis of $CO_2$ laser cutting", *Proceeding of the Institute of Mechanical Engineers, Part B*, Vol. 211, pp. 223-32.

Yilbas, B.S. and Sahin, A.Z. (1994), "Turbulent boundary layer approach allowing chemical reactions for $co_2$ laser oxygen-assisted cutting process", *Proceedings Institution of Mechanical Engineers*, Vol. 208, pp. 275-84.